# Nanoscale

Check for updates

# New opportunities for efficient N$_2$ fixation by nanosheet photocatalysts

Hao Li, [ID] Chengliang Mao, Huan Shang, Zhiping Yang, Zhihui Ai and Lizhi Zhang [ID] *

Catalytic ammonia synthesis from dinitrogen (N$_2$) under mild conditions has been considered to be the "holy grail" of N$_2$ fixation, which is one of the most important chemical processes in the agriculture, biological and industrial fields. Given that current artificial N$_2$ fixation is still dominated by the energy-intensive Haber−Bosch process, solar N$_2$ fixation represents an encouraging and fascinating route for carbon-free and energy-saving N$_2$ fixation. However, its practical application is seriously hampered by surface sluggish reaction kinetics. In this minireview, we share our perspectives on the use of two-dimensional (2D) nanosheets for the manipulation of photocatalytic N$_2$ fixation. Nanosheet photocatalysts serve as the perfect platform for the engineering of surface active sites, including defects and iron, all of which can not only bolster photon−exciton interaction toward robust charge carriers generation upon light absorption, but also mimic the function schemes of MoFe-cofactor in nitrogenase toward sufficient N$_2$ binding and activation. These merits endowed by nanosheets photocatalysts provide instructive information on exploring the rich nitrogen photochemistry on solid surfaces and offer new opportunities for the design of novel photocatalysts towards efficient N$_2$ fixation.

## 1. Introduction

Naturally occurring N$_2$ fixation has failed to meet the demands of fertilizer industry in modern times due to explosion of the world's population, making it critical to pursue artificial N$_2$ fixation technology.[1,2] The first pioneering large-scale N$_2$ fixation industry was discovered and advanced by Fritz Haber and Carl Bosch using metal catalysts in the early 1990s. For now, Haber–Bosch process constitutes a key part of earth nitrogen circle and generates 450 million tons of fixed nitrogen a year.[3] Unfortunately, positive impacts of industrial N$_2$ fixation are counterbalanced by its energy-intensive nature. Nonpolar N$_2$ has a strong N–N triple bond, high ionization energy, and negative electron affinity.[4] This is the reason why Haber–Bosch process has to be carried out under harsh condition, necessitating both red-hot temperature (300–600 °C) and high pressure (150–250 atm). Besides, Haber–Bosch requires pure H$_2$ as the feedstock, which is typically supplied from the energy-consuming reaction of methane steam reforming. As a consequence, such a H$_2$ production process consumes nearly 2% of the annual global supply with a considerable amount of global greenhouse gas being released.[1] Therefore, the develop-ment of a sustainable N$_2$ fixation strategy has been a demanding and compelling challenge.

In stark contrast to industrial Haber–Bosch process, nature accomplishes N$_2$ fixation through nitrogenase enzymes in certain bacteria under ambient temperature and pressure. The large difference in the reaction condition between industrial and biological N$_2$ fixation raises the question as to why nitrogenase is superior to Haber–Bosch catalysts. The most common nitrogenase complex is composed of two proteins that work collectively: homodimeric Fe protein and heterotetrameric MoFe protein.[5] Homodimeric Fe protein possesses a high reducing power to supply electrons while the heterotetrameric MoFe protein manipulates the electrons provided to reduce N$_2$ to NH$_3$ (Fig. 1a).[6] The key center residing in MoFe protein is the FeMo-cofactor, which is capable of binding, activation and reduction of N$_2$. Although the precise mechanistic
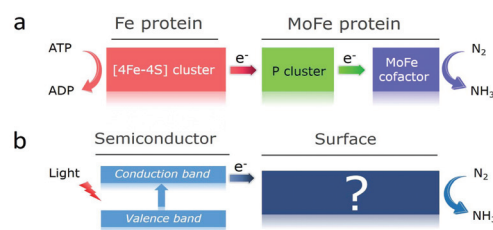
*Key Laboratory of Pesticide & Chemical Biology of Ministry of Education, Institute of Environmental & Applied Chemistry, College of Chemistry, Central China Normal University, Wuhan 430079, P. R. China. E-mail: zhanglz@mail.ccnu.edu.cn; Fax: +86-27-67867535; Tel: +86-27-6786 7535*

**Fig. 1** Schematic illustration of fundamental processes of (a) biological and (b) photocatalytic N$_2$ fixation.

details are unclear for now, biological $N_2$ fixation is still a touchstone and representative model for the development of alternative routes to the Haber–Bosch process by constructing functional models with nitrogenase-like activity.

## 2.  Photocatalytic $N_2$ fixation

Similar to nitrogenase, semiconductor-based photocatalysis can also achieve $N_2$ fixation under ambient temperature and pressure. This strategy is very promising due to $H_2$ not being used, and as inexhaustible solar energy and water can provide active electrons and protons for direct $N_2$ fixation.[7] However, contemporary photocatalytic $N_2$ fixation still suffers from poor quantum yield. The first obstacle limiting the photocatalytic $N_2$ fixation efficiency arises from the poor interfacial charge transfer that leads to intensive electron–hole recombination, manifesting a weak photon–exciton interaction towards the exciton dissociation.[8] The second obstacle can be ascribed to the poor energetics of photogenerated electrons. This fact can be exemplified by the direct or proton-coupled one-electron $N_2$ reduction ($N_2 + e^- \rightarrow N_2^-{}_{(aq)}$, −4.2 V vs. NHE; $N_2 + H^+ + e^- \rightarrow N_2H$, −3.2 V vs. NHE), both of which are not energetically possible for electrons of most semiconductors.[9] Considering the function mode nitrogenase, the reason why biological $N_2$ fixation process appears less "up-hill" can be attributed to the enhanced binding and activation of $N_2$ on the MoFe-cofactor. In the light of this point, chemists have been attempting to activate the strong N–N triple bond through coordinating $N_2$ to the unsaturated transition metal complexes (metal = Fe, Mo, Ru and Co) for stoichiometrically transforming coordinated $N_2$ into $NH_3$ or $N_2H_4$.[10] Photocatalytic $N_2$ fixation differs from homogeneous $N_2$ reduction by transition metal complexes or MoFe-cofactor as it is a chemical process occurring on the surface of semiconductors. Hence, its catalytic efficiency is intrinsically related to the surface chemistry of semiconductors. Therefore, it is of great significance to fabricate semiconductors with well-designed surface catalytic sites to ensure efficient charge carriers generation and also mimic the functionality of MoFe-protein for the N–N triple bond activation to improve the overall $N_2$ fixation efficiency (Fig. 1b).

## 3.  Two-dimensional (2D) nanosheets photocatalysts

Recently, 2D nanosheets catalysts have attracted considerable research attention because of their novel electrical, optical, electronic and mechanical properties, which have found wide applications in energy and environmental fields. Meanwhile, nanosheet photocatalysts can also act as a good model to gain deep insights into the correlations between atomic/electronic structures and their intrinsic properties, as summarized by several pioneering reviews.[11–13] As for photocatalysis, nanosheets enable facile surface functionality towards the formation of active sites. First, surface defects, can be easily created on nanosheets with well-engineered surface bond length, dangling bond and disorder degree. Second, nanosheets provide an ultrahigh surface area for the loading of active co-catalysts. As for photocatalytic $N_2$ fixation, surface defects and co catalysts are able to influence charge carrier kinetics and also affect the kinetics of the surface reaction.

We share our perspectives on the use of 2D nanosheets for the manipulation of photocatalytic $N_2$ fixation in this minireview. According to the published results, new opportunities can be opened by nanosheets for efficient photocatalytic $N_2$ fixation. This is because nanosheets photocatalysts can be used as the perfect platform for the engineering of surface active sites, including defects and iron, all of which have been shown to bolster photon–exciton interactions resulting in the generation of facile charge carriers upon light absorption. In addition, they also mimic the roles of MoFe-cofactor in nitrogenase to achieve sufficient $N_2$ binding and activation.

## 4.  Nanosheets photocatalysts for $N_2$ fixation

### 4.1  Oxygen defects of bismuth oxyhalides

Oxygen vacancies (OVs) are the most widely studied and common surface anion defects on oxide surfaces possessing low formation energy. According to our previous results, on a prototypical ternary oxide material of BiOBr, OVs influenced photocatalytic $N_2$ fixation in two ways.[14] First, the presence of OVs inhibited the electron–hole recombination, according to the enhanced defects emission in the steady-state photoluminescence (PL) spectra, thus facilitating photon–exciton interaction toward robust charge carriers generation via trapping hot electrons (Fig. 2a and b). Interestingly, in the $N_2$ atmosphere, such a PL peak was remarkably quenched due to the accelerated interfacial transfer from BiOBr to $N_2$. This phenomenon was closely related to another role played by OVs for reliable $N_2$ activation. OVs are coordinating unsaturated centers for direct $N_2$ adsorption, and also prominently electron-rich centers with localized electrons capable of activating N–N triple bond via a charge back-donation (Fig. 2c). As supported by density functional theory (DFT) calculations, instant $N_2$ activation was evidenced by an increased N–N bond length of 1.133 Å between the N–N triple bond (1.078 Å) and double bond (1.201 Å). Since $N_2$ could be activated on OVs, which was similar to that on MoFe-cofactor in nitrogenase, efficient $N_2$ fixation was expected due to the facile electron transfer from OVs to the $\pi$ antibonding orbital of $N_2$. According to the work reported by Ye et al., a similar $N_2$ activation scheme could also be realized on the OVs of $Bi_5O_7Br$, an important derivative of BiOBr with a novel light-switchable OVs generation characteristic (Fig. 2d).[15]

To shed light on the influence of different OV structures on $N_2$ fixation, and clarify the detailed mechanistic steps of photocatalytic $N_2$ fixation, we employed BiOCl nanosheets with two surface exposure models as the model photocatalysts.[16,17] $N_2$ exhibited a terminal end-on adsorption structure on the OV of BiOCl (001) surface, while on the OV of the (010)
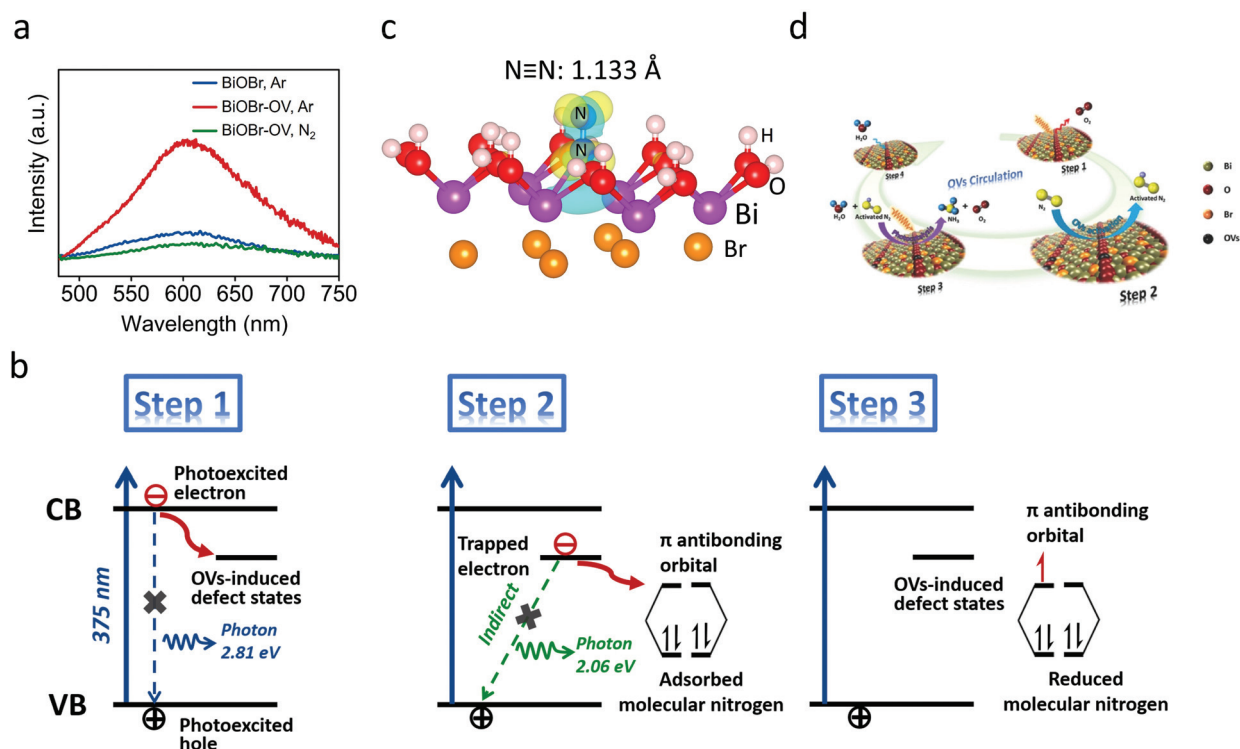
**Fig. 2** (a) Steady PL spectra of the as-synthesized BiOBr in different atmosphere. (b) Schematic illustration for OVs-associated interfacial electron transfer for $N_2$ fixation. (c) Terminal end-on adsorption structure of $N_2$ on the OV of BiOBr. (d) Schematic illustration of light-switchable OVs generation for $N_2$ fixation on $Bi_5O_7Br$. Reprinted with permission from ref. 14 and 15.

surface, it was in a side-on bridging adsorption mode (Fig. 3a and b). On the OV of BiOCl (001) surface, the triple N–N bond was activated to 1.137 Å, while on the OV of the (010) surface it was further elongated to 1.198 Å; close to the value of N–N double bond of $N_2H_2$ (1.201 Å).

Two widely-accepted mechanisms are proposed over photocatalytic $N_2$ fixation: distal and alternating.[18,19] In the distal

mechanism, hydrogenation of the uncoordinated N atom in $N_2$ occurs consecutively to form a terminal nitride intermediate, generating the first $NH_3$ molecule. Then, the single coordinated N will be converted into another $NH_3$ molecule (Scheme 1). In contrast, in the alternating mechanism, hydrogenation occurs alternately on the two coordinating N atoms of $N_2$, generating key intermediates like metal-bound diazene (HN=NH) and hydrazine ($H_2N–NH_2$) (Scheme 1). Theoretical calculation further revealed that fixation of $N_2$ in a terminal end-on coordination structure was expected to proceed via an asymmetrically distal pathway, in which $N_2$ fixation preferentially occurred on the N atom away from the OV (Fig. 3c). Coordinating N began to be fixed only after distant N was fully hydrogenated. The fixation of $N_2$ in the side-on bridging mode was achieved via a symmetrically alternative pathway because both the coordinating N atoms shared the same possibility
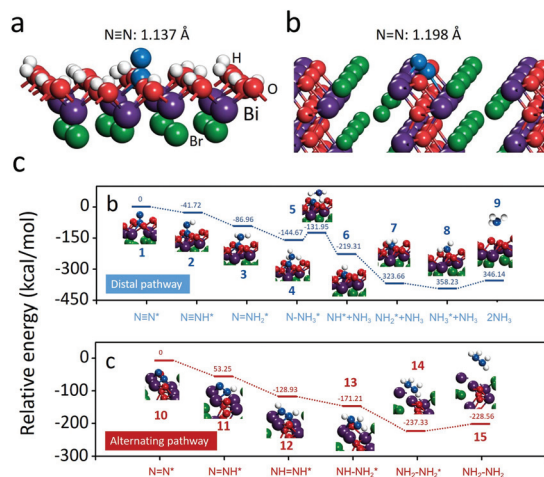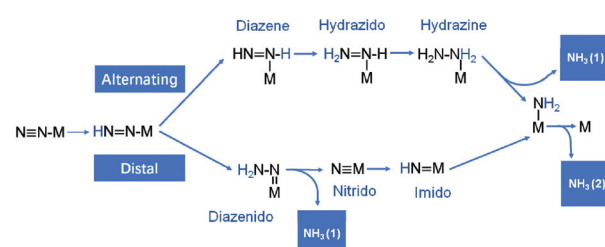


**Fig. 3** $N_2$ adsorption structures on the OV of (a) BiOCl(001) and (b) BiOCl(010) surface. (c) OV-mediated $N_2$ fixation pathways. Reprinted with permission from ref. 16.



**Scheme 1** Distal and alternating pathway for $N_2$ fixation.

towards hydrogenation, thus generating possible intermediates, including $N_2H_2$ and $N_2H_4$ (Fig. 3c). Noticeably, in contrast with uncatalyzed free $N_2$ fixation which faced high thermodynamic barriers towards the formation of $N_2H_2$ or $N_2H_4$, $N_2$ fixation on the BiOCl(001) or (010) surface was thermodynamically accessible due to the presence of molecular steps in low energy created by surface OV. Intrinsic thermodynamically promoted $N_2$ fixation occurred due to the increase in the Lewis acid/base reactivity upon activation, thus speeding the subsequent electron transfer and proton attack in water.

## 4.2 Oxygen defects of layered-double-hydroxide

Layered-Double-Hydroxides (LDH) are a new class of promising 2D photocatalysts, because both the constituent metal cation and thickness can be tuned for band structure engineering (Fig. 4a). Zhang *et al.* proposed that OVs or coordinately unsaturated sites could be easily generated when the size of LDH nanosheets was controlled to a few nanometers.[20] Well-designed CuCr-LDH nanosheets (CuCr-NS) were synthesized, in which $Cr^{3+}$ showed strong absorption to visible light, while $Cu^{2+}$ acted as the divalent cation to promote defects formation. According to the Cr K-edge extended X-ray absorption near-edge fine structures (EXAFS), distance of first shell Cr–O bond length was around 1.1989 Å, much shorter than that observed on conventionally synthesized bulk CuCr-LDH (CuCr-Bulk) because of the severe structure distortion around the Cr cations, which could be explained by the structural compression in the *ab*-plane in the presence of OVs (Fig. 4b and c). As for photocatalytic $N_2$ fixation in water, CuCr-NS exhibited superior activity than the bulk counterpart under visible light (Fig. 4d). Presence of OVs within CuCr-NS strongly affected its photocatalytic $N_2$ fixation performance in two ways. First, OVs introduced prominent defect levels to the CuCr-LDH bandgap with compressive strain, arisen from unoccupied Cr 3d orbitals. These new energy states strengthen photon–exciton interaction *via* promoting the light response region of CuCr-LDH and facilitating the electron–hole separation. Second, OVs increased $N_2$ adsorption energy and also activated the N–N bond like MoFe-cofactor for kinetically enhanced $N_2$ reduction after photoexcitation.

Similar OV-mediated efficient sunlight-driven nitrogen fixation could be also achieved over ultrathin $TiO_2$ nanosheets and $Bi_2MoO_6$, another Bi based nanosheet. Using OVs as the $N_2$ activation sites and plasmonic Au as the hot electrons source, Yang *et al.* achieved a high apparent quantum efficiency of 0.82% at 550 nm for $N_2$ fixation.[21] Dong *et al.* purposely introduced unsaturated Mo atoms on the edge *via* oxygen defects through hydrogenation.[22] According to the $N_2$ reduction curves, hydrogenated $Bi_2MoO_6$ (H-$Bi_2MoO_6$) was demonstrated to drive $N_2$ fixation under low working potential of 0.36 V *vs.* SCE, much lower than that of conventional $Bi_2MoO_6$ (C-$Bi_2MoO_6$) without defects (Fig. 4e).

## 4.3 Nitrogen vacancies

Nitrogen vacancies (NVs) are common defects observed in graphite carbon nitride (g-$C_3N_4$), a metal-free 2D polymeric photocatalyst consisting of repeating units of tris-triazine in each layer and van-der-Waals force between layers. Similar to OVs, NVs have also been demonstrated to largely improve the photocatalytic performances of g-$C_3N_4$ by extending its photoresponse, promoting charge carriers separation and enhancing reactant adsorption.[23–26] Due to the metal-free polymeric character of g-$C_3N_4$ with the diverse nitrogen environment, tuning of NVs during synthesis is more facile than that of OVs. Niu *et al.* introduced NVs located at $N_{2c}$ lattice sites *via* controlling the polycondensation temperature. g-$C_3N_4$ with NVs displayed enhanced light absorption, restrained charge carriers' recombination and improved performance to generate ·OH radicals.[23] Hong *et al.* prepared nitrogen-deficient g-$C_3N_4$ *via* a hydrothermal treatment using ammonium thiosulfate as an oxidant and improved the photocatalytic $H_2$ evolution rate of pristine g-$C_3N_4$ 2 fold.[24] Ding *et al.* found presence of NVs within the framework of $C_3N_4$ due to the loss of $NH_x$ species displayed improved reactivity for the aerobic oxidation of aromatic alcohols to aldehydes under simulated sunlight.[25] The concept of NVs for possible $N_2$ activation was introduced by Dong *et al.*[27] They suggested that NVs could behave like a $N_2$-imprinted polymer due to its size being similar to that of the N atom in $N_2$. Enhanced adsorption and activation of $N_2$ on NVs was therefore expected. Besides, NVs could also trap photoexcited electrons to facilitate the generation of charge carriers just like OVs. NVs were introduced *via* simply calcining g-$C_3N_4$ at 520 °C under a $N_2$ flow for 2 h (Fig. 5a). Control
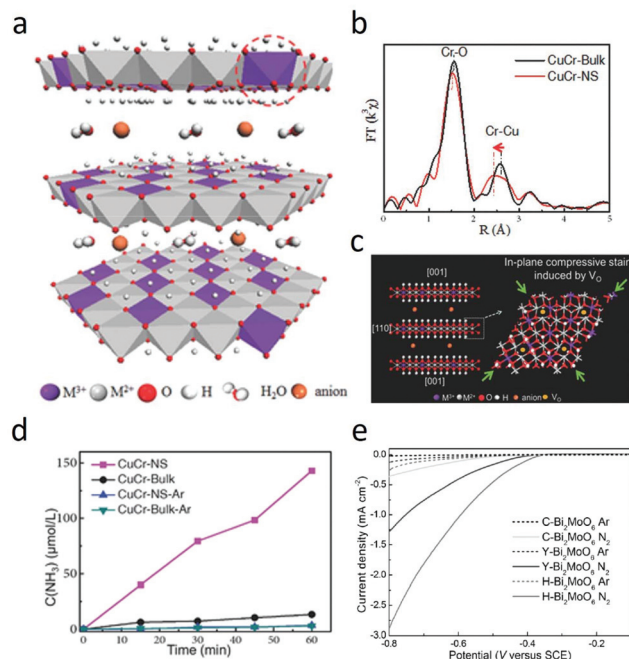


**Fig. 4** (a) Schematic illustration of the ultrathin LDH structure. (b) $k^2$-weighted FT of Cr K-edge EXAFS spectra. (c) Schematic of the in-plane biaxial compressive strain in CuCr-NS. (d) Photofixation of $N_2$ fixation over the as-prepared CuCr-LDH in different atmosphere. (e) $N_2$ reduction and HER polarization curves for H-$Bi_2MoO_6$ in comparison with C-$Bi_2MoO_6$. Reprinted with permission from ref. 20 and 22.
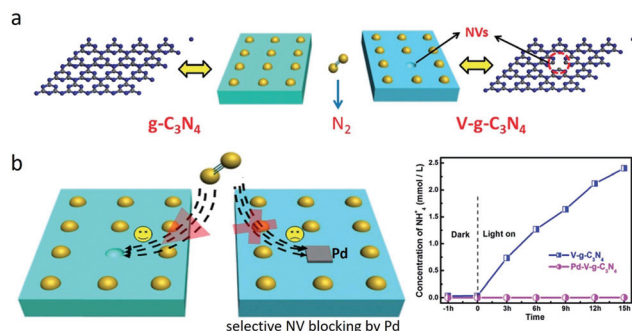
**Fig. 5** (a) Preparation process for $C_3N_4$ with NVs. (b) NVs site blocking by Pd particles for suppressed photocatalytic $N_2$ fixation. Reprinted with permission from ref. 27.

experiments revealed that $NH_4^+$ could not be generated without visible light or NVs. $^{15}N_2$ isotopic labelling experiment further proved that $N_2$ was the source of the formed $NH_4^+$. The strong chemical $N_2$ adsorption was associated with $N_2$ activation, as proven by increased N–N bond length (from 1.117 Å to 1.214 Å) according to DFT calculation. Meanwhile, selective block of NVs using metallic Pd completely suppressed the photocatalytic $N_2$ fixation performance of V-g-$C_3N_4$, further confirming $N_2$ was mainly adsorbed and reduced on NVs (Fig. 5b). g-$C_3N_4$ has also been recently demonstrated to be a reliable 2D component for the synthesis of nanocomposites, including $C_3N_4$/MgAlFeO, $C_3N_4$/graphene oxide, $C_3N_4$/$W_{18}O_{49}$, $C_3N_4$/$Ga_2O_3$, etc., all of which could realize efficient charge carrier separation and photocatalytic $N_2$ fixation.[28–31] Unfortunately, the decomposition of g-$C_3N_4$ would bring false positive results of $NH_4^+$ generation, which could not be ruled out by $^{15}N_2$ isotopic labelling experiments. This phenomenon should be carefully considered when some nitrogen containing photocatalysts or sacrificial reagents are used for photocatalytic $N_2$ fixation in the future.

### 4.4 Iron (Fe)

Fe, either in its cation state or metal state, is the key element for biological and industrial $N_2$ fixation. For instance, the preparation of Fe-based metal complexes for $N_2$ activation is inspired by the fine structure of FeMo-cofactor, and metallic Fe directly activates $N_2$ towards dissociation under certain conditions.[32,33] In photocatalysis, iron doping or loading is a universal strategy to enhance photocatalytic performances of many semiconductor materials, including $N_2$ fixation. The feasibility of $N_2$ binding and reduction on Fe was first theoretically evaluated by Azofra and his co-workers.[34] Using a 2D $MoS_2$ as the platform, they theoretically proposed a hybrid structure, where single Fe atoms are deposited on the basal planes of 2H-$MoS_2$, mimicking the FeMo-cofactor (Fig. 6a). Bader charge analysis revealed a net charge transfer from Fe to $MoS_2$, making Fe a plausible binding site for lone pairs of $N_2$. Nature of $N_2$–Fe interaction was directly relevant to two major spontaneous $d(Fe) \rightarrow \pi^*(N_2)$ charge transfers responsible for the N–N triple bond elongation to 1.14 Å (Fig. 6b).
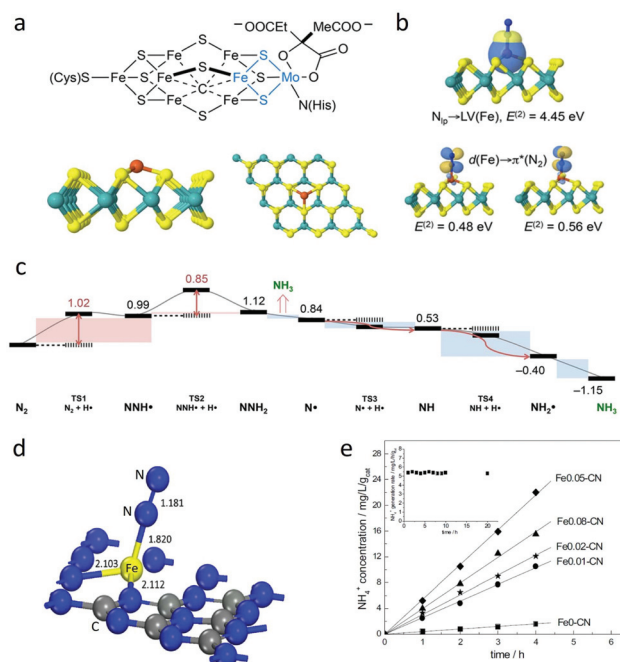


**Fig. 6** (a) Schematic illustration of nitrogenase FeMo cofactor and optimized Fe deposited on 2D $MoS_2$. (b) Adsorption $N_2$ on surface Fe atom of Fe–$MoS_2$ and the corresponding interfacial charge transfer process. (c) Minimum Gibbs free energy path corresponding to $N_2$ conversion into $NH_3$ catalyzed by Fe deposited on $MoS_2$. (d) Optimized $N_2$ adsorption Fe-doped $C_3N_4$. (e) Influence of Fe concentration on the photocatalytic $N_2$ fixation performance of $C_3N_4$. Reprinted with permission from ref. 34 and 35.

Broader theoretical calculations suggested the $N_2$ fixation over Fe–$MoS_2$ would be realized under mild condition and that the rate-determining step is the first $H^+/e^-$ pair with a 1.02 eV energy barrier along with complete $N_2$ hydrogenation to $NH_3$ (Fig. 6c). Using $C_3N_4$ as the substrate, Wu et al. directly prepared a $Fe^{3+}$-doped $C_3N_4$ (Fe–CN) and evaluated its photocatalytic performance for $N_2$ fixation.[35] $Fe^{3+}$ was found to be directly inserted into the interstitials and was stabilized by $C_3N_4$ with an electron-rich character through the covalent Fe–N bond. Physical $N_2$ adsorption on pristine $C_3N_4$ was accompanied by release of $-14.6$ kJ $mol^{-1}$ energy, while direct chemisorption of $N_2$ on Fe was evidenced by a large adsorption energy of $-134.8$ kJ $mol^{-1}$ with a lengthened N–N triple bond of 1.181 Å (Fig. 6d). As for the $N_2$ fixation, Fe–CN with an optimized Fe loading amount showed 13.5-fold higher rate than that of undoped $C_3N_4$ (Fig. 6e).

Besides $MoS_2$ and $C_3N_4$, graphene was also demonstrated to be an excellent promoter for $N_2$ fixation. Graphene is single-layered graphite and attracted enormous interest since its discovery due to its excellent mechanical, thermal and electric properties. It can be used as the perfect substrate for the development of functionalized nanocomposites for new applications. Recently, graphene is demonstrated to reach a reverse saturation state with abundant hot electrons above the Fermi level under visible light.[36] Following this discovery, Chen et al.
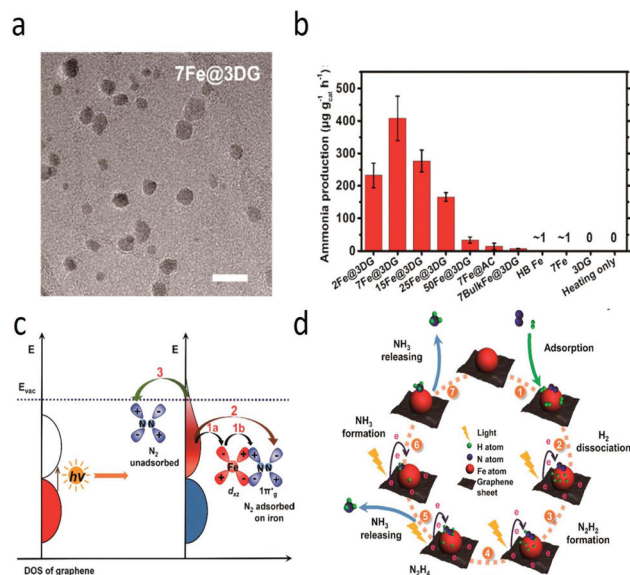
**Fig. 7** (a) TEM image of a typical Fe@3DG nanocomposite. (b) Catalytic performance of Fe@3DG with different Fe loading under atmospheric pressure. (c) Proposed three paths of the hot electrons from light illuminated graphene toward prompted $N_2$ activation. (d) Proposed mechanism for $NH_3$ synthesis on Fe@ 3DG. Reprinted with permission from ref. 37.

took full advantage of the light-induced energetic hot electrons from graphene as the direct reducing species to fix $N_2$ under mild conditions.[37] They intentionally loaded iron oxide on a 3D cross-linked graphene material to synthesize a Fe@3DGraphene (Fe@3DG) nanocomposite (Fig. 7a). Under ambient conditions, Fe@3DG was able to synthesize $NH_3$ using a $H_2/N_2$ (3/1) mixture gas and an optimized $N_2$ fixation could be realized *via* tuning the iron loading amount (Fig. 7b). Remarkable $N_2$ fixation only happened under a certain threshold light intensity where reverse saturation state of graphene was simultaneously achieved. After the threshold, hot electron injection and $N_2$ fixation increased along with light intensity increase. Hot electrons of graphene can increase the electron density of the loaded Fe nanoparticles, or get

indirectly captured by $N_2$ *via* a tunneling path, or directly get transferred to $N_2$ adsorbed on graphene (Fig. 7c). Chen *et al.* proposed a general reaction mechanism associating the N–N dissociation enabled by a synergetic effect between iron and hot electrons of graphene, which proceeded through the intermediates of $N_2H_2$ and $N_2H_4$ (Fig. 7d).

Table 1 summarizes the photocatalytic activities of as-mentioned nanosheets photocatalysts for $N_2$ reduction, which are not totally unified due to different experimental conditions, including light source, temperature, and concentration of the photocatalysts. Hopefully, apparent quantum yield may be generalized as a comparison standard in the future.

## 5. Summary and outlook

In this minireview, we share our perspectives on the use of 2D nanosheets for the manipulation of photocatalytic $N_2$ fixation by summarizing the results reported by our group and other groups. We firmly believe new opportunities can be opened by nanosheets for efficient photocatalytic $N_2$ fixation for two aspects. First, photon–exciton interaction toward facile charge carrier generation upon light absorption can be bolstered. Second, the surface active sites can mimic the function schemes of MoFe-cofactor in nitrogenase toward sufficient $N_2$ adsorption and activation. These merits endowed by nanosheets photocatalysts provide instructive information on exploring the rich nitrogen photochemistry on solid surfaces and offer new opportunities for the design of novel 2D photocatalysts towards efficient $N_2$ fixation. Despite many advantages of solar ammonia synthesis without the use of electricity or heat, it is also faced with grand challenges. For instance, produced ammonia can be further oxidized to nitrite or nitrate or photogenerated holes or activated oxygen, which can be circumvented if photocatalytic reactors can be designed well so as to separate these oxidative species with ammonia. Meanwhile, atomistic insights into fundamental mechanisms of photocatalytic $N_2$ fixation is still in the early stage and require a combination of theoretical calculations and modern *in situ* characterization techniques, including TEM, XPS and FTIR. Moreover, rational engineering of surface active sites on

**Table 1** Summary of nanosheet photocatalysts for the reduction of $N_2$ to $NH_3$

| Catalyst | Reaction medium | Light source | Scavenger | Ammonia generation rate |
|---|---|---|---|---|
| BiOBr[14] | $H_2O$ | $\lambda > 420$ nm | None | 104.2 µmol $g^{-1}$ $h^{-1}$ |
| $Bi_5O_7Br$[15] | $H_2O$ | $\lambda > 400$ nm | None | 1380 µmol $g^{-1}$ $h^{-1}$ |
| BiOCl[16] | $H_2O$ | Full spectrum | Methanol | 92.4 µmol $g^{-1}$ $h^{-1}$ |
| CuCr-NS[20] | $H_2O$ | Full spectrum | none | 184.8 µmol $g^{-1}$ $h^{-1}$ |
| $Au/TiO_2$-OV[21] | $H_2O$ | Full spectrum | Methanol | 78.6 µmol $g^{-1}$ $h^{-1}$ |
| $H-Bi_2MoO_6$[22] | $H_2O$ | Full spectrum | none | 1.3 µmol $g^{-1}$ $h^{-1}$ |
| $V-g-C_3N_4$[27] | $H_2O$ | $\lambda > 420$ nm | Methanol | 160 µmol $g^{-1}$ $h^{-1}$ |
| $C_3N_4/MgAlFeO$[28] | $H_2O$ | 400–800 nm | Ethanol | 417 µmol $g^{-1}$ $h^{-1}$ |
| $C_3N_4/W_{18}O_{49}$[29] | $H_2O$ | Full spectrum | Ethanol | 144.5 µmol $g^{-1}$ $h^{-1}$ |
| $C_3N_4$/graphene oxide[30] | $H_2O$ | Full spectrum | Ethylenediaminetetraacetic acid | 515 µmol $g^{-1}$ $h^{-1}$ |
| $C_3N_4/Ga_2O_3$[31] | $H_2O$ | Full spectrum | Ethanol | 281.2 µmol $g^{-1}$ $h^{-1}$ |
| $Fe-C_3N_4$[35] | $H_2O$ | $\lambda > 420$ nm | None | 325 µmol $g^{-1}$ $h^{-1}$ |
| Fe@3DG[37] | $H_2$&$N_2$, 473 K | UV | None | 24 µmol $g^{-1}$ $h^{-1}$ |

2D photocatalysts is essential to maximize the overall photocatalytic $N_2$ fixation, and also enable the understanding of the active sites–catalytic activity relationship. We believe this mini-review will be helpful to researchers in the area of photocatalysis and $N_2$ fixation.

## Conflicts of interest

There are no conflicts to declare.

## Acknowledgements

## Notes and references

1  A. J. Medford and M. C. Hatzell, *ACS Catal.*, 2017, **7**, 2624–2643.
2  X. Chen, N. Li, Z. Kong, W.-J. Ong and X. Zhao, *Mater. Horiz.*, 2018, **5**, 9–27.
3  V. Smil, *Nature*, 1999, **400**, 415–415.
4  C.-G. Zhan, J. A. Nichols and D. A. Dixon, *J. Phys. Chem. A*, 2003, **107**, 4184–4195.
5  B. K. Burgess and D. J. Lowe, *Chem. Rev.*, 1996, **96**, 2983–3012.
6  D. R. Dean, J. T. Bolin and L. Zheng, *J. Bacteriol.*, 1993, **175**, 6737–6744.
7  G. N. Schrauzer and T. D. Guth, *J. Am. Chem. Soc.*, 1977, **99**, 7189–7193.
8  S. Bai, J. Jiang, Q. Zhang and Y. Xiong, *Chem. Soc. Rev.*, 2015, **44**, 2893–2939.
9  D. Zhu, L. Zhang, R. E. Ruther and R. J. Hamers, *Nat. Mater.*, 2013, **12**, 836–841.
10  H.-P. Jia and E. A. Quadrelli, *Chem. Soc. Rev.*, 2014, **43**, 547–564.
11  Y. Sun, S. Gao, F. Lei and Y. Xie, *Chem. Soc. Rev.*, 2015, **44**, 623–636.
12  Y. Liu, C. Xiao, Z. Li and Y. Xie, *Adv. Energy Mater.*, 2016, 1600436.
13  Y. Sun, S. Gao, F. Lei, C. Xiao and Y. Xie, *Acc. Chem. Res.*, 2015, **48**, 3–12.
14  H. Li, J. Shang, Z. Ai and L. Zhang, *J. Am. Chem. Soc.*, 2015, **137**, 6393–6399.
15  S. Wang, X. Hai, X. Ding, K. Chang, Y. Xiang, X. Meng, Z. Yang, H. Chen and J. Ye, *Adv. Mater.*, 2017, **29**, 1701774.
16  H. Li, J. Shang, J. Shi, K. Zhao and L. Zhang, *Nanoscale*, 2016, **8**, 1986–1993.
17  H. Li, J. Li, Z. Ai, F. Jia and L. Zhang, *Angew. Chem., Int. Ed.*, 2018, **57**, 122–138.
18  D. Lukoyanov, S. A. Dikanov, Z.-Y. Yang, B. M. Barney, R. I. Samoilova, K. V. Narasimhulu, D. R. Dean, L. C. Seefeldt and B. M. Hoffman, *J. Am. Chem. Soc.*, 2011, **133**, 11655–11664.
19  C. Guo, J. Ran, A. Vasileff and S.-Z. Qiao, *Energy Environ. Sci.*, 2018, **11**, 45–56.
20  Y. Zhao, Y. Zhao, G. I. N. Waterhouse, L. Zheng, X. Cao, F. Teng, L.-Z. Wu, C.-H. Tung, D. O'Hare and T. Zhang, *Adv. Mater.*, 2017, **29**, 1703828.
21  J. Yang, Y. Guo, R. Jiang, F. Qin, H. Zhang, W. Lu, J. Wang and J. C. Yu, *J. Am. Chem. Soc.*, 2018, **140**, 8497–8508.
22  Y. Hao, X. Dong, S. Zhai, H. Ma, X. Wang and X. Zhang, *Chem. – Eur. J.*, 2016, **22**, 18722–18728.
23  P. Niu, G. Liu and H.-M. Cheng, *J. Phys. Chem. C*, 2012, **116**, 11013–11018.
24  Z. Hong, B. Shen, Y. Chen, B. Lin and B. Gao, *J. Mater. Chem. A*, 2013, **1**, 11754–11761.
25  J. Ding, W. Xu, H. Wan, D. Yuan, C. Chen, L. Wang, G. Guan and W.-L. Dai, *Appl. Catal., B*, 2018, **221**, 626–634.
26  Q. Tay, P. Kanhere, C. F. Ng, S. Chen, S. Chakraborty, A. C. H. Huan, T. C. Sum, R. Ahuja and Z. Chen, *Chem. Mater.*, 2015, **27**, 4930–4933.
27  G. Dong, W. Ho and C. Wang, *J. Mater. Chem. A*, 2015, **3**, 23435–23441.
28  S. Cao, N. Zhou, F. Gao, H. Chen and F. Jiang, *Appl. Catal., B*, 2017, **218**, 600–610.
29  S. Hu, W. Zhang, J. Bai, G. Lu, L. Zhang and G. Wu, *RSC Adv.*, 2016, **6**, 25695–25702.
30  Y. Wang, W. Wei, M. Li, S. Hu, J. Zhang and R. Feng, *RSC Adv.*, 2017, **7**, 18099–18107.
31  H. Liang, H. Zou and S. Hu, *New J. Chem.*, 2017, **41**, 8920–8926.
32  K. Arashiba, Y. Miyake and Y. Nishibayashi, *Nat. Chem.*, 2011, **3**, 120–125.
33  R. Schlögl, *Angew. Chem., Int. Ed.*, 2003, **42**, 2004–2008.
34  L. M. Azofra, C. Sun, L. Cavallo and D. R. MacFarlane, *Chem. – Eur. J.*, 2017, **23**, 8275–8279.
35  S. Hu, X. Chen, Q. Li, F. Li, Z. Fan, H. Wang, Y. Wang, B. Zheng and G. Wu, *Appl. Catal., B*, 2017, **201**, 58–69.
36  D. Brida, A. Tomadin, C. Manzoni, Y. J. Kim, A. Lombardo, S. Milana, R. R. Nair, K. S. Novoselov, A. C. Ferrari, G. Cerullo and M. Polini, *Nat. Commun.*, 2013, **4**, 1987.
37  Y. Lu, Y. Yang, T. Zhang, Z. Ge, H. Chang, P. Xiao, Y. Xie, L. Hua, Q. Li, H. Li, B. Ma, N. Guan, Y. Ma and Y. Chen, *ACS Nano*, 2016, **10**, 10507–10515.